Composite Structures 391 (2026) 120544

Contents lists available at ScienceDirect

Composite Structures

journal homepage: www.elsevier.com/locate/compstruct

Lamination parameter informed encoder–decoder framework for stiffness tailoring in composite lattices

Jagan Selvaraj *, Sondipon Adhikari [1]

Glasgow Computational Engineering Centre (GCEC)
James Watt School of Engineering, The University of Glasgow, Glasgow G12 8QQ, UK

ARTICLE INFO

Keywords:
Lamination parameters
Physics-informed neural networks
Composite lattices
Inverse design
Anisotropy tailoring

ABSTRACT

Composite lattices, periodic architectures of interconnected fibre-reinforced members, offer exceptional stiffness-to-weight ratios critical for aerospace light-weighting and net-zero emission strategies, yet their directional property tailoring remains underexploited due to design complexity. Composite lattice optimisation confronts a fundamental combinatorial challenge: the design space grows exponentially with ply count, requiring exhaustive searches across ply moduli, fibre orientations, layup sequences, and geometric parameters that rapidly become intractable for multifunctional structural tailoring. We introduce a physics-informed encoder–decoder architecture that circumvents this dimensional curse by projecting the discrete optimisation problem into a continuous latent space of lamination parameters. The encoder, implemented as a feed-forward neural network, maps target homogenised elastic moduli (E_x, E_y) to member-level lamination parameters, while the decoder embeds closed-form analytical expressions from classical laminate theory and homogenisation mechanics. This architecture eliminates data dependency and ensures physical consistency throughout the inverse design process. By minimising reconstruction loss between predicted and target properties, the framework learns physically realisable lamination parameter combinations that simultaneously satisfy stiffness targets and manufacturing constraints for balanced, symmetric laminates. Applied to hexagonal composite lattices, the method reveals that maximum achievable anisotropy depends not only on fibre-matrix modulus contrast but fundamentally scales with lattice effective stiffness, establishing material-dependent upper bounds ranging from 1.03 for E-glass to 1.49 for high-modulus carbon systems. The framework enables rapid exploration of previously inaccessible design regions, reduces inverse design from iterative numerical optimisation to direct analytical mapping, and provides a generalisable template for integrating domain-specific physics with machine learning in structural design.

1. Introduction

The design of lightweight and high-performance structures remains a cornerstone in aerospace engineering, where reductions in structural mass directly translate to improved energy efficiency and payload capacity [1,2]. Achieving such light-weighting goals is critical in the broader context of net-zero emission strategies [3]. Lattice structures, characterised by periodic arrangements of interconnected struts or unit cells, offer a compelling solution due to their ability to deliver high stiffness-to-weight ratios [4,5]. These architectures, composed of members primarily loaded in tension or compression, enable efficient load transfer while minimising material usage, a quality highly advantageous in aerospace structures ranging from satellite frames to morphing skins [6–8].

Composite lattice structures are a promising class of lightweight architectures that combine the directional tailoring capabilities of fibre-reinforced composites with the structural efficiency of periodic lattices [9,10]. However, the corresponding design problem is challenging. The effective properties of a composite lattice depend on the longitudinal and transverse properties, ply orientation, ply count and thickness. As the number of plies increases, the number of possible stacking sequences grows combinatorially and makes multi-query optimisation challenging [11].

To accelerate design iterations it is essential to have an efficient homogenisation framework. Analytical methods, to compute the equivalent properties of lattice, and Representative Volume Element (RVE) approaches are versatile methods used in the literature for homogenisation [12–14]. Analytical methods typically assume a 1D or 2D

* Corresponding author.
E-mail addresses: Jagan.Selvaraj@glasgow.ac.uk (J. Selvaraj), Sondipon.Adhikari@glasgow.ac.uk (S. Adhikari).
[1] Professor of Engineering Mechanics.

https://doi.org/10.1016/j.compstruct.2026.120544
Received 13 January 2026; Received in revised form 6 May 2026; Accepted 10 June 2026
Available online 15 June 2026

representation of lattice members and the deformation behaviour, to enable computation of stiffness via force–deflection or strain–energy based approaches [15]. RVE methods are typically implemented via Finite Element Method (FEM) and can be applied to periodic and non-periodic lattices [16]. Efficient homogenisation methods can make the forward calculation of computing equivalent stiffness faster. However, a major challenge with these methods is that the design dimension remains constant and thus the inverse design is challenging.

Lamination parameters provide a method to mitigate this combinatorial explosion by projecting discrete stacking variables into a continuous, low-dimensional representation of composite properties [17,18], while admissible stacking sequences need to be recovered in a post-processing step. They are used in designing variable stiffness composite structures [19], post-buckling optimisation [20] and doubly curved composite plates [21]. While the forward mapping from lamination parameters to effective responses such as E_x, E_y is analytically tractable, the inverse mapping from target responses to admissible lamination parameters is potentially non-unique, and constrained by manufacturing rules.

Some studies are presented in the literature to address the aspects of this challenge in inverse design. Ntourmas et al. [22] proposed a mixed-integer linear programming formulation for retrieving manufacturable stacking sequences from lamination parameters, enforcing blending and continuity rules directly. Sprengholz et al. [23] developed a rapid transformation method to convert lamination parameters into stacking sequences, reducing the computational overhead of sequence retrieval. At the functional level, Riley et al. [24] demonstrated inverse design of bistable laminates for morphing applications, illustrating how inverse methods can enable programmable behaviour. When compared to surrogate-based approaches and direct inverse methods, physics-constrained and theory-guided ML models embedding laminate mechanics have improved data efficiency, robustness, and interpretability, accelerating practical composite inverse design (Li et al. 2024).

Machine learning has emerged as a suitable choice to develop fast surrogates for optimisation and thereby can enable inverse design. In the absence of vast amount of data, physics-informed neural networks can be trained directly on the governing equations and the associated boundary conditions and physical quantities are enforced by minimising a loss function [25]. Surrogate-based approaches approximate high-fidelity simulations and are coupled with optimisation or Bayesian frameworks to efficiently explore large laminate design space [26]. Direct inverse methods using generative models, such as variational autoencoders, address the non-uniqueness of inverse problems by producing multiple feasible designs for a given target response [25,27]. Li et al. [27] introduced a physics-constrained deep learning approach for identifying material parameters in laminates.

Wang et al. [28] introduced a data-driven inverse method that uses Gaussian Process Regression to accurately identify fibre path parameters in variable stiffness laminates accounting for manufacturing uncertainties. Sun et al. [29] provided an efficient inverse design framework for composite layups using a variational autoencoder. Zhou et al. [30] developed a topology optimisation approach for composite lattices with mutiple morphology, where the material density is first optimised and then mapped to lattice cells with tailored anisotropic stiffness. Peng et al. [31] introduced an inverse design method for bi-material composite lattice structures using artificial neural networks.

Despite these advances, the design of composite lattices by integrating lamination parameter for dimension reduction with physics-informed learning remains underexplored. This paper addresses this gap by introducing a lamination parameter-informed encoder–decoder framework for the inverse design of composite lattices. The encoder is a neural network that maps target global elastic moduli (E_x, E_y) into a latent space of lamination parameters. This is regarded as a predictor step where the initial set of lamination parameters is corrected by a decoder. The decoder is not data-driven but a differentiable physics module that incorporates analytical expressions for member stiffness and homogenisation rules, ensuring that reconstructed properties $(\hat{E}_x, \hat{E}_y)$ remain accurate and physically valid. By minimising the distance between the target and the reconstructed moduli, the required lamination parameters are retrieved. Manufacturing constraints are enforced post-prediction to design balanced and symmetric laminates. Stacking sequences are then efficiently retrieved using a kd-tree search in lamination parameter space.

We introduce a normalised anisotropy measure and derive an upper bound on anisotropy achievable under laminate theory. The key contributions of this work are:

- The development of analytical equations using lamination parameters to calculate homogenised lattice properties.
- The formulation of lamination parameter-informed encoder–decoder framework to perform inverse design efficiently.
- The incorporation of manufacturing constraints and the integration of stacking-sequence retrieval through kd-tree structure.
- Applications of the framework to anisotropy tailoring, derivation of a normalised anisotropy measure and the identification of upper bounds.

The paper is organised as follows. Section 2 derives closed-form expressions for the equivalent elastic properties of heterogeneous hexagonal lattices. Section 3 reformulates these expressions in terms of lamination parameters by invoking classical laminate plate theory. The physics-informed encoder–decoder architecture is presented in Section 4. Section 5 verifies the lamination parameter formulation against literature benchmarks and visualises the feasible design space. Section 6 demonstrates inverse design capability, showing how the trained framework predicts manufacturable layups that satisfy prescribed stiffness targets while respecting balanced and symmetric laminate constraints through kd-tree retrieval. Section 7 focuses on anisotropy tailoring, deriving analytical expressions for the anisotropy ratio as a function of material and geometric parameters, examining material selection criteria, and establishing upper bounds on achievable directional stiffness contrast for different composite systems. Conclusions and directions for future work are provided in Section 8.

2. Unit cell analysis of a heterogeneous lattice

To demonstrate the unit cell analysis of a heterogeneous lattice, consider the hexagonal lattice shown in Fig. 1, where the unit cell has three different members with unique composite properties. The equivalent elastic properties of this composite lattice can be calculated using plane stress assumptions. Each member has its unique properties, and the homogenised elastic modulus and thickness of these members are given by E_a, t_a (for member a), E_b, t_b (for member b) and E_c, t_c (for member c). This results in the equivalent properties Eqs. (1)–(5) of the composite lattice [32]. The subscripts in the equation below indicate the properties in the global x- and y-directions. Modifying h and θ can lead to distinct lattice types as observed in [33]. Therefore the results presented here can be generalised for other lattice types.

The equations for the equivalent properties are derived by assuming the member deformation behaviour and follows Castigliano's theorem to calculate the directional member stiffness (x and y). Since the analytical derivation of these equations can be referred in the literature with changes for the composite member properties, the derivation of the equations are not explicitly shown. In the rest of the section, equations are suitably rearranged to improve their understanding and the corresponding plots are also shown.

The equivalent homogenised properties of the hexagonal lattice described in Fig. 1 can be calculated using the Eqs. (1)–(5). E_x and E_y are the equivalent longitudinal and transverse modulus, ν_{xy} and ν_{yx} are Poisson's ratio measured when loaded in x and y directions, and G_{xy} is the equivalent shear modulus.

$$E_x = \frac{2\alpha^3 \cos\theta}{(\beta + \sin\theta)\left[\sin^2\theta\left(\frac{1}{E_a} + \frac{1}{E_b}\right) + \alpha^2\cos^2\theta\left(\frac{1}{E_a} + \frac{1}{E_b}\right)\right]} \tag{1}$$

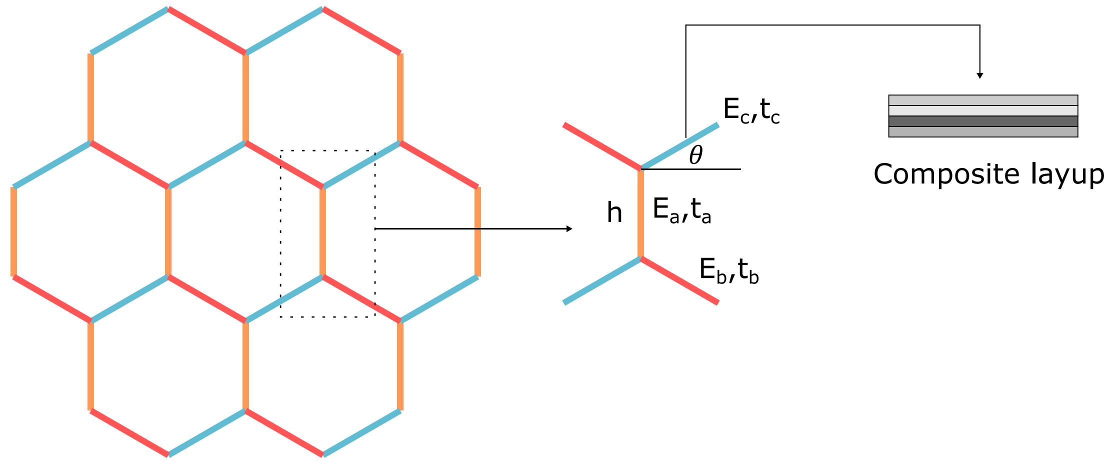

Fig. 1. Hexagonal lattice unit cell geometry comprises three member types with independent composite layups: inclined members a and b (length L, angle θ) and vertical member c (height h). Each member has homogenised elastic modulus E_m and thickness t_m ($m = a, b, c$).

$$E_y = \frac{2\alpha^3(\beta+\sin\theta)}{\cos^3\theta\left(\frac{1}{E_a}+\frac{1}{E_b}\right)+\alpha^2\sin^2\theta\cos\theta\left(\frac{1}{E_a}+\frac{1}{E_b}\right)+\alpha^2\cos\theta\frac{4\beta}{E_c}} \tag{2}$$

$$\nu_{xy} = \frac{\cos^2\theta\left[\left(\frac{1}{E_a}+\frac{1}{E_b}\right)-\alpha^2\left(\frac{1}{E_a}+\frac{1}{E_b}\right)\right]}{(\beta+\sin\theta)\sin\theta\left[\left(\frac{1}{E_a}+\frac{1}{E_b}\right)+\alpha^2\cot^2\theta\left(\frac{1}{E_a}+\frac{1}{E_b}\right)\right]} \tag{3}$$

$$\nu_{yx} = \frac{\sin\theta(\beta+\sin\theta)\left[\left(\frac{1}{E_a}+\frac{1}{E_b}\right)-\alpha^2\left(\frac{1}{E_a}+\frac{1}{E_b}\right)\right]}{\cos^2\theta\left(\frac{1}{E_a}+\frac{1}{E_b}\right)+\alpha^2\sin^2\theta\left(\frac{1}{E_a}+\frac{1}{E_b}\right)+\alpha^2\frac{4\beta}{E_c}} \tag{4}$$

$$G_{xy} = \frac{4\alpha^3(\beta+\sin\theta)}{\cos\theta\left[\beta^2\left(\frac{1}{E_a}+\frac{1}{E_b}\right)+\alpha^2\left(\cos\theta+(\beta+\sin\theta)\tan\theta\right)^2\left(\frac{1}{E_a}+\frac{1}{E_b}\right)+\frac{4\beta^3}{E_c}\right]} \tag{5}$$

In the above equations, it is assumed that the thickness of all the members is the same, that is, $t_a = t_b = t_c = t$ (say). The non-dimensional parameters α and β are defined as

$$\alpha = \frac{t}{L} \quad \text{and} \quad \beta = \frac{h}{L} \tag{6}$$

Same thickness is assumed because stiffness tailoring is demonstrated later across lattices with same geometry.

Using these, the relative density of the lattice can be obtained as

$$\rho_r = \frac{\rho}{\rho_s} = \frac{\alpha(2+\beta)}{2\cos\theta(\beta+\sin\theta)} \tag{7}$$

where ρ_s is the average density of a constituent composite material. Note that the relative density is a function of the geometry of the lattice only.

For analytical simplifications, we introduce two further non-dimensional parameters quantifying the disparities between the elastic modulus of the three composite elements in the lattice. They are defined as

$$\eta_1 = \frac{E_b}{E_a} \quad \text{and} \quad \eta_2 = \frac{E_c}{E_a} \tag{8}$$

and these are called as the material disparity ratios. These quantities can be substituted in the expressions of the equivalent properties of the lattice above for further simplification of the analytical expressions as

$$E_x = E_a \cdot \frac{\eta_1}{1+\eta_1} \cdot \frac{2\alpha^3\cos\theta}{(\beta+\sin\theta)} \cdot \frac{1}{\sin^2\theta+\alpha^2\cos^2\theta} \tag{9}$$

$$E_y = E_a \frac{\eta_1}{1+\eta_1} \cdot \frac{2\alpha^3(\beta+\sin\theta)}{\cos\theta} \cdot \frac{1}{\cos^2\theta+\alpha^2\sin^2+\alpha^2\frac{4\beta}{\eta_2}\cdot\frac{\eta_1}{1+\eta_1}} \tag{10}$$

$$\nu_{xy} = \frac{\cos^2\theta(1-\alpha^2)}{(\beta+\sin\theta)\sin\theta(1+\alpha^2\cot^2\theta)} \tag{11}$$

$$\nu_{yx} = \frac{\sin\theta(\beta+\sin\theta)(1-\alpha^2)}{\left(\cos^2\theta+\alpha^2\sin^2\theta\right)+\alpha^2\frac{4\beta}{\eta_2}\cdot\frac{\eta_1}{1+\eta_1}} \tag{12}$$

$$G_{xy} = E_a \cdot \frac{\eta_1}{1+\eta_1} \cdot \frac{4\alpha^3(\beta+\sin\theta)}{\cos\theta} \cdot \frac{1}{\beta^2+\alpha^2(\cos\theta+(\beta+\sin\theta)\tan\theta)^2+\frac{4\beta^3}{\eta_2}\cdot\frac{\eta_1}{1+\eta_1}} \tag{13}$$

The material disparity ratios $\eta_1 = \frac{E_b}{E_a}$ and $\eta_2 = \frac{E_c}{E_a}$ quantify the stiffness contrast between the primary material E_a and the secondary materials E_b and E_c, respectively. When $\eta_1 \ll 1$, corresponding to a compliant secondary phase, the lattice exhibits a pronounced reduction in its equivalent stiffnesses E_x, E_y, and G_{xy}. In the opposite limit, $\eta_1 \to \infty$, the stiffer constituent dominates, and the effective moduli asymptotically approach those of the primary phase E_a. Similar behaviour can be observed for η_2 The combined influence of η_1 and η_2, together with the geometry parameters α and β, determines the balance between axial and shear deformation mechanisms and thus governs the transition from a flexible anisotropic lattice to a stiffer, nearly isotropic structural configuration.

Fig. 2 illustrates the contours of the normalised equivalent modulus plotted as a function of the material disparity ratio η_1 and the cell angle θ for $\alpha = 0.2$. Two representative cases are shown corresponding to ($\beta = 1, \eta_2 = 1$) and ($\beta = 2.5, \eta_2 = 0.2$). The results reveal that the equivalent modulus E_x and E_y increases nonlinearly with η_1 and is sensitive to both the cell geometry and height ratio. For larger β, the influence of η_1 becomes more pronounced, indicating stronger coupling between geometric configuration and stiffness contrast among the lattice members. The contour corresponding to $\eta_1 = \eta_2 = 1$ and $\theta = 30°$ represents the baseline case of a homogeneous regular lattice. This provides a reference configuration for interpreting how introducing stiffness contrasts (i.e., $\eta_1 \neq 1$, $\eta_2 \neq 1$) can enhance or diminish anisotropic mechanical responses.

Figs. 2(e) and 2(f) reveal that the shear stiffness is more sensitive to geometric variation than the axial moduli, particularly at smaller θ values where the inclined members dominate the load transfer. Increasing η_1 enhances G_{xy} up to a saturation point, beyond which geometric effects prevail.

3. Lamination parameters for lattices

In this section, the equivalent properties of lattices are derived in terms of lamination parameters, which express global mechanical quantities, such as stiffness, in terms of material invariants and

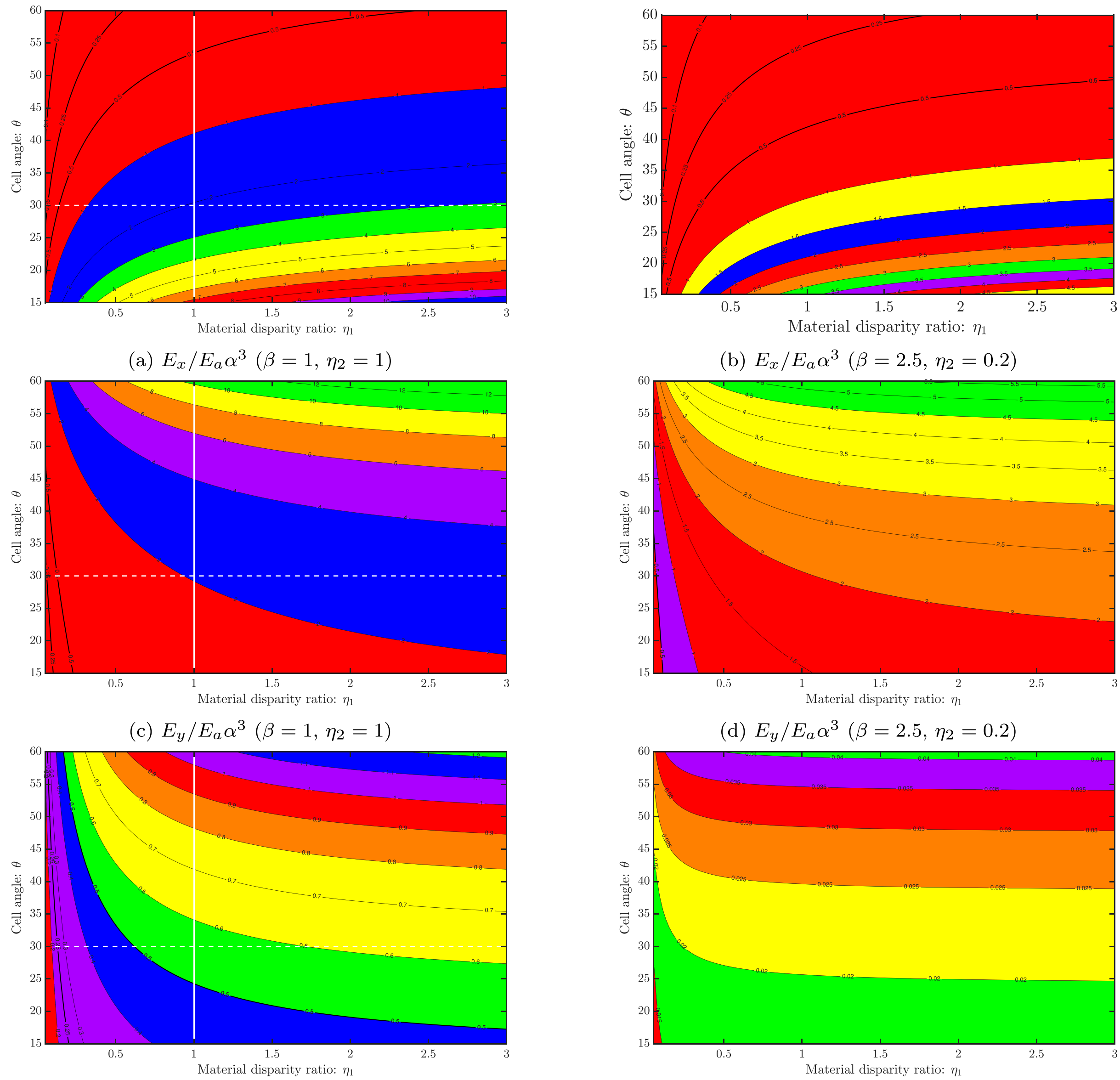

(a) $E_x/E_a\alpha^3$ ($\beta = 1$, $\eta_2 = 1$)

(b) $E_x/E_a\alpha^3$ ($\beta = 2.5$, $\eta_2 = 0.2$)

(c) $E_y/E_a\alpha^3$ ($\beta = 1$, $\eta_2 = 1$)

(d) $E_y/E_a\alpha^3$ ($\beta = 2.5$, $\eta_2 = 0.2$)

(e) $G_{xy}/E_a\alpha^3$ ($\beta = 1$, $\eta_2 = 1$)

(f) $G_{xy}/E_a\alpha^3$ ($\beta = 2.5$, $\eta_2 = 0.2$)

Fig. 2. Contours of normalised E_x, E_y, G_{xy} plotted as functions of the material disparity ratio (η_1) and the cell angle (θ) for $\alpha = 0.2$ and different values of the height ratio (β) and material disparity ratio η_2. The case corresponding to the classical single-material regular homogeneous lattice ($\beta = \eta_1 = \eta_2 = 1$, $\theta = 30°$) is marked with lines in 2(a), 2(c) and 2(e).

direction-dependent terms [34]. Lamination parameters acts as a solution to reduce the problem complexity especially when the design space is large. This can be quickly demonstrated with Fig. 3. Here the number of feasible laminates (symmetric and balanced) is plotted against the number of plies (function of thickness). In this semi-log plot, the laminate design space rises with the number of plies.

One of the key global properties of interest in lattice structures is the longitudinal stiffness and can be represented in a simplified form as:

$$E_x = f(\mathbf{U})g(\xi) \tag{14}$$

where $\mathbf{U}$ denotes a material invariant that encapsulates the intrinsic stiffness of the lamina, and $g(\xi)$ is a function of the lamination parameters which encode the orientation distribution of plies throughout the laminate thickness.

Under plane stress conditions, typically assumed for thin laminates or lattice members, the constitutive behaviour of an orthotropic lamina is described by the reduced stiffness matrix $\mathbf{Q}$ which relates in-plane stresses to in-plane strains:

$$Q_{11} = \frac{E_{11}}{1 - \nu_{12}\nu_{21}} \qquad Q_{22} = \frac{E_{22}}{1 - \nu_{12}\nu_{21}} \tag{15}$$

$$Q_{12} = \frac{\nu_{12}E_{22}}{1 - \nu_{12}\nu_{21}} = \frac{\nu_{21}E_{11}}{1 - \nu_{12}\nu_{21}} \qquad Q_{66} = G_{12} \tag{16}$$

where E_{11} is the longitudinal modulus, E_{22} is the transverse modulus, G_{12} is the shear modulus, and ν_{12} is Poisson's ratio expressed in material coordinate system.

Following classical laminate plate theory for multi-ply laminates the global stiffness behaviour can be described using the ABD stiffness matrix, which accounts for extensional, coupling, and bending effects. For symmetric laminates, the coupling matrix $\mathbf{B}$ vanishes, leading to a decoupling of extension and bending. The in-plane extensional behaviour is then fully characterised by the $\mathbf{A}$ matrix, with

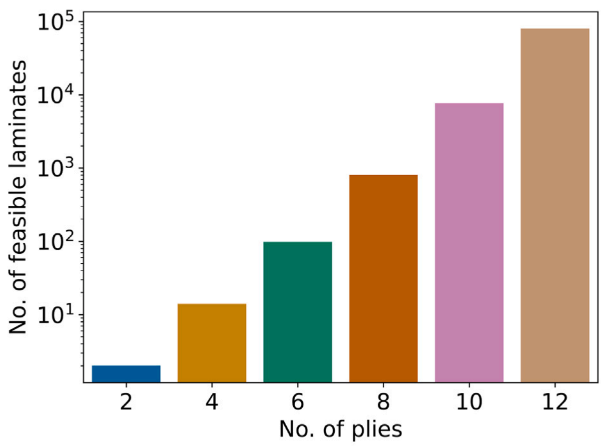

Fig. 3. Combinatorial explosion of symmetric and balanced laminate design space with increasing ply count.

components:

$$A_{ij} = \sum_{k=1}^{n} \left(\bar{Q}_{ij}\right)_k (h_k - h_{k-1}) \tag{17}$$

where h_k and h_{k-1} are the distances from the laminate mid-plane to the top and bottom of the kth ply, n is the number of plies, and Q_{ij} is the transformed reduced stiffness matrix of the kth ply.

A matrix in terms of lamination parameters is given by,

$$\begin{bmatrix} A_{11} \\ A_{12} \\ A_{22} \\ A_{66} \\ A_{16} \\ A_{26} \end{bmatrix} = t \begin{bmatrix} 1 & \xi_1 & \xi_2 & 0 & 0 \\ 0 & 0 & -\xi_2 & 1 & 0 \\ 1 & -\xi_1 & \xi_2 & 0 & 0 \\ 0 & 0 & -\xi_2 & 0 & 1 \\ 0 & \frac{\xi_3}{2} & \xi_4 & 0 & 0 \\ 0 & \frac{\xi_3}{2} & -\xi_4 & 0 & 0 \end{bmatrix} \begin{bmatrix} U_1 \\ U_2 \\ U_3 \\ U_4 \\ U_5 \end{bmatrix}$$

where t is the total laminate thickness, ξ_m are the lamination parameters, and **U** are material invariants.

The material invariants are given by

$$U_1 = \frac{1}{8}\left(3Q_{11} + 3Q_{22} + 2Q_{12} + 4Q_{66}\right) \tag{18}$$

$$U_2 = \frac{1}{2}\left(Q_{11} - Q_{22}\right) \tag{19}$$

$$U_3 = \frac{1}{8}\left(Q_{11} + Q_{22} - 2Q_{12} - 4Q_{66}\right) \tag{20}$$

$$U_4 = \frac{1}{8}\left(Q_{11} + Q_{22} + 6Q_{12} - 4Q_{66}\right) \tag{21}$$

$$U_5 = \frac{1}{8}\left(Q_{11} + Q_{22} - 2Q_{12} + 4Q_{66}\right) \tag{22}$$

The lamination parameters ξ_m are defined as:

$$\xi_1 = \frac{1}{t}\int_{-t/2}^{t/2} \cos 2\Theta(z)\,dz = \frac{1}{t}\sum_{k=1}^{n} \cos\left(2\Theta_k\right)\,(h_{k-1} - h_k), \tag{23}$$

$$\xi_2 = \frac{1}{t}\int_{-t/2}^{t/2} \cos 4\Theta(z)\,dz = \frac{1}{t}\sum_{k=1}^{n} \cos\left(4\Theta_k\right)\,(h_{k-1} - h_k), \tag{24}$$

$$\xi_3 = \frac{1}{t}\int_{-t/2}^{t/2} \sin 2\Theta(z)\,dz = \frac{1}{t}\sum_{k=1}^{n} \sin\left(2\Theta_k\right)\,(h_{k-1} - h_k), \tag{25}$$

$$\xi_4 = \frac{1}{t}\int_{-t/2}^{t/2} \sin 4\Theta(z)\,dz = \frac{1}{t}\sum_{k=1}^{n} \sin\left(4\Theta_k\right)\,(h_{k-1} - h_k), \tag{26}$$

Here Θ is the fibre orientation at a distance z from the mid-plane. The integral above is a general definition and is converted to finite sum since laminated composite thickness distribution is piecewise continuous. The feasible design space in terms of lamination parameters for symmetric and balanced laminates are shown in Fig. 5. It is worth mentioning that only symmetric and balanced laminates are considered since they reduce the shrinkage during curing and are widely preferred.

The equivalent elastic modulus can be computed from the **A** matrix by computing its inverse. However, to perform this simplified calculation, **B** needs to be zero necessating the presence of balanced and symmetric laminates. The **A** matrix of such laminates with $A_{16} = A_{26} = 0$ is given by

$$\mathbf{A} = \begin{bmatrix} A_{11} & A_{12} & 0 \\ A_{12} & A_{22} & 0 \\ 0 & 0 & A_{66} \end{bmatrix} \tag{27}$$

The determinant of **A** and cofactor of A_{11} is,

$$\det(\mathbf{A}) = A_{66}.(A_{11}A_{22} - A_{12}A_{21}) \tag{28}$$

$$\text{cofactor}(A_{11}) = A_{22}A_{66} \tag{29}$$

The equivalent elastic modulus of a lattice member $m = a, b, c$ can then be calculated from the A matrix as:

$$E_m = \frac{1}{t}\left(\frac{1}{A_{11}^{-1}}\right) = \frac{1}{t}\left(\frac{A_{66}.(A_{11}A_{22} - A_{12}A_{21})}{A_{22}A_{66}}\right) \tag{30}$$

$$E_m = \frac{1}{t}\left(\frac{A_{11}A_{22} - A_{12}^2}{A_{22}}\right) \tag{31}$$

The components of **A** in terms of lamination parameters are given as,

$$A_{11} = t(U_1 + \xi_1 U_2 + \xi_2 U_3) \tag{32}$$

$$A_{12} = t(-\xi_2 U_3 + U_4) \tag{33}$$

$$A_{22} = t(U_1 - \xi_1 U_2 + \xi_2 U_3) \tag{34}$$

$$A_{66} = t(-\xi_2 U_3 + U_5) \tag{35}$$

By substituting the components of **A** into Eq. (31), a closed-form relation for the equivalent modulus in terms of the design variables is obtained, enabling efficient analytical optimisation.

$$E_m = \frac{1}{t}\left(\frac{t^2(U_1 + \xi_1 U_2 + \xi_2 U_3)(U_1 - \xi_1 U_2 + \xi_2 U_3) - t^2(-\xi_2 U_3 + U_4)^2}{t(U_1 - \xi_1 U_2 + \xi_2 U_3)}\right) \tag{36}$$

$$E_m = \frac{U_1^2 + 2\xi_2 U_1 U_3 - (\xi_1 U_2)^2 + 2\xi_2 U_3 U_4 - U_4^2}{U_1 - \xi_1 U_2 + \xi_2 U_3} \tag{37}$$

By substituting Eq. (37) into Eqs. (1)–(5), the homogenised lattice properties can be obtained. It is important to note that each lattice member ($m = a, b, c$) can have a distinct composite layup, characterised by its own set of lamination parameters ($\xi_1^{(m)}, \xi_2^{(m)}$) to obtain E_a, E_b, and E_c.

This hierarchical design process establishes a direct pathway from ply-level design variables to lattice-level effective properties. However, the inverse mapping from target member moduli to lamination parameters involves navigating a non-unique solution space. For a given target modulus E_m, multiple lamination parameter pairs ($\xi_1^{(m)}, \xi_2^{(m)}$) may satisfy Eq. (37) due to the coupled nonlinear relationship between material invariants and lamination parameters. Furthermore, the material invariants (U_1, U_2, U_3, U_4, U_5) vary across composite systems, meaning that different materials require distinct lamination parameter combinations to achieve the same elastic modulus. This multiplicity of solutions offers designers flexibility to satisfy secondary constraints such as manufacturability, buckling resistance, or failure margins.

4. Lamination-parameter informed encoder–decoder

To infer the underlying lamination parameters of a composite laminate from its macroscopic elastic properties, we developed a encoder–decoder framework based on a fully connected neural network architecture. The model maps the effective in-plane Young's moduli (E_x, E_y) to six latent lamination parameters $\boldsymbol{\xi} = [\xi_1^a, \xi_2^a, \xi_1^b, \xi_2^b, \xi_1^c, \xi_2^c]$ corresponding to three laminate members (a, b, c).

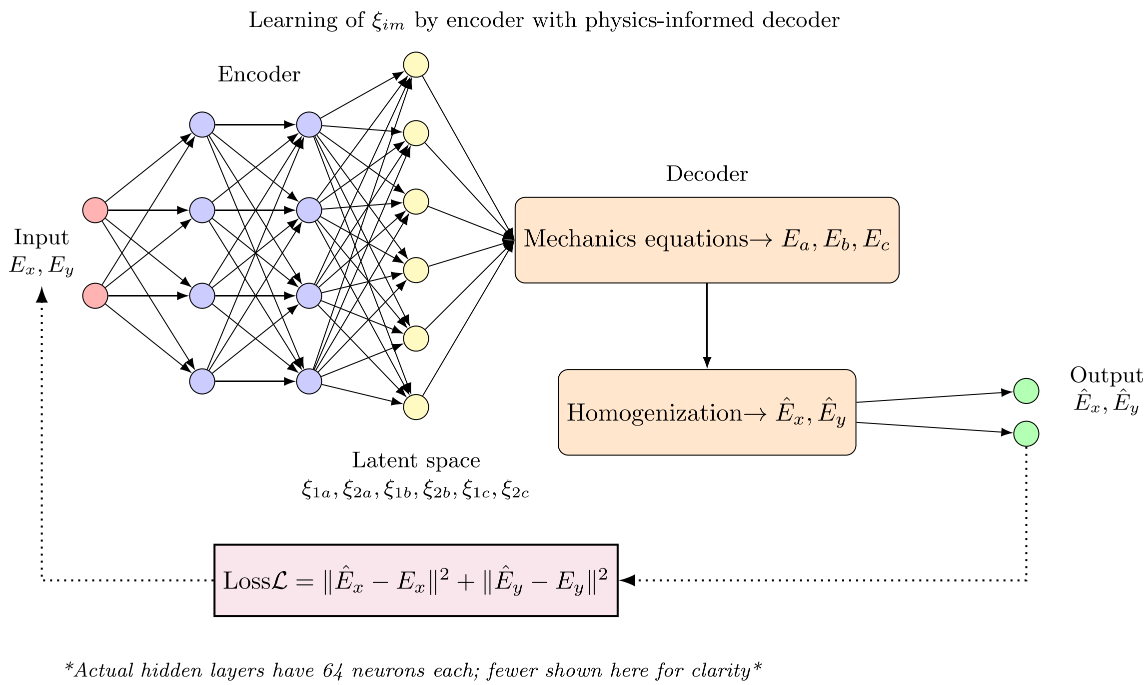

Fig. 4. Architecture of physics-informed encoder–decoder framework for inverse design of composite lattices. Actual hidden layers contain 64 neurons each; fewer shown for clarity.

4.1. Model architecture

The encoder is a feed-forward neural network with two hidden layers of 64 neurons each and hyperbolic tangent (tanh) activations. It maps the input vector $\mathbf{x} = [E_x, E_y] \in \mathbb{R}^2$ to the lamination parameter vector $\boldsymbol{\xi} \in [-1, 1]^6$ via

$$\boldsymbol{\xi} = \tanh(f_\Gamma(\mathbf{x})), \tag{38}$$

where f_Γ denotes the neural network with trainable parameters Γ. This model architecture is shown in Fig. 4

4.2. Physics-based decoding

The predicted lamination parameters are used in an analytical model to compute the directional Young's moduli E_a, E_b, and E_c of the three members. Each modulus is given by a closed-form expression derived in Eq. (37):

$$E_i = \frac{U_1^2 - 2\xi_2^i U_1 U_3 - (\xi_1^i U_2)^2 + 2\xi_2^i U_3 U_4 - U_4^2}{U_1 - \xi_1^i U_2 + \xi_2^i U_3 + \epsilon}, \quad i \in \{a, b, c\},$$

where U_1, U_2, U_3, U_4 and U_5 are material invariants and ϵ is a small regularisation term to ensure numerical stability.

4.3. Homogenisation model

The homogenised in-plane elastic moduli $(E_x^{\text{pred}}, E_y^{\text{pred}})$ are then calculated using expressions that depend on the member-wise moduli and geometric parameters:

$$E_x^{\text{pred}} = \frac{2\cos\theta}{(\beta + \sin\theta)\left[\sin^2\theta\left(\frac{1}{E_a a_1^3} + \frac{1}{E_b a_2^3}\right) + \cos^2\theta\left(\frac{1}{E_a a_1} + \frac{1}{E_b a_2}\right)\right]},$$

$$E_y^{\text{pred}} = \frac{2(\beta + \sin\theta)}{\cos\theta\left[\cos^2\theta\left(\frac{1}{E_a a_1^3} + \frac{1}{E_b a_2^3}\right) + \sin^2\theta\left(\frac{1}{E_a a_1} + \frac{1}{E_b a_2}\right) + \frac{4\beta}{E_c a_3}\right]},$$

where θ is the lattice angle, β is the aspect ratio h/L, and a_1, a_2, a_3 are relative thicknesses of the laminate members.

4.4. Loss function

The model is trained by minimising the discrepancy between the predicted and true values of the effective moduli:

$$\mathcal{L} = \left(E_x^{\text{pred}} - E_x\right)^2 + \left(E_y^{\text{pred}} - E_y\right)^2. \tag{39}$$

As the prediction of the encoder–decoder improves, the loss minimises and approaches convergence. Physically, this means that the mechanical principles and design targets will be achieved without requiring homogenisation training data.

4.5. Characteristics of the network

This model incorporates closed-form constitutive equations and homogenisation rules, ensuring that the predicted outputs rely on the mechanics. The use of the tanh activation function constrains the lamination parameters to the physically meaningful range $[-1, 1]$, which improves interpretability. Each latent variable corresponds to a specific lamination parameter, enabling direct physical insight into the network's predictions. This combination of data-driven learning and embedded physical laws enhances the accuracy, and generalisation of the model across different number of plies and layups (symmetric and balanced).

4.6. Layup reconstruction from predicted lamination parameters

Following the prediction of lamination parameters by the encoder–decoder framework, the corresponding stacking sequences (layups) are reconstructed by querying a precomputed database of candidate layups and their associated lamination parameters. This is an exhaustive database of all possible symmetric and balanced sequences for a given ply count. For each target set of predicted lamination parameters, k-d tree (pre-trained) is employed to identify the nearest neighbour in lamination parameter space based on the Euclidean distance. This procedure is applied to all target vectors, and the total distance across all targets is accumulated for each candidate k-d tree structure.

$$\text{Total distance} = \sqrt{\sum_i \left\|\xi_i^{\text{pred}} - \xi_i^{\text{db}}\right\|^2},$$

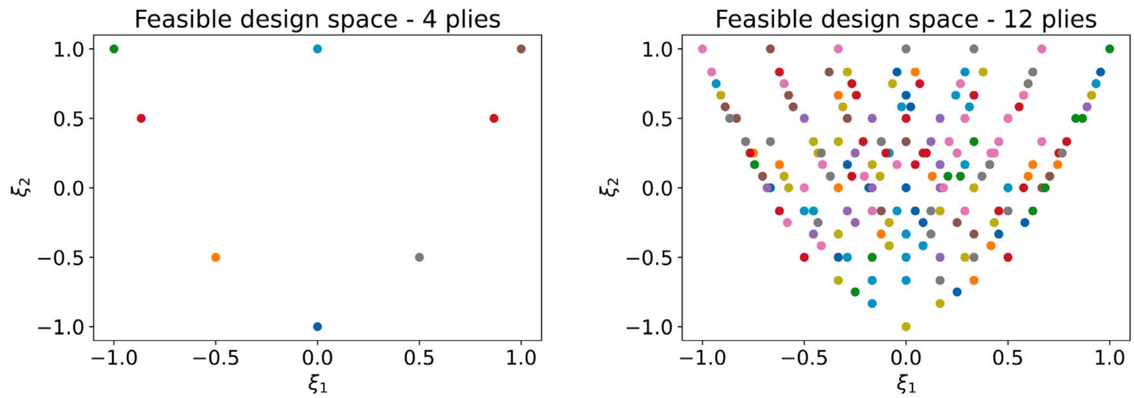

(a) 4 Plies (b) 12 Plies

Fig. 5. Feasible design space of symmetric and balanced laminates in lamination parameter coordinates (ξ_1, ξ_2) for (a) 4-ply and (b) 12-ply configurations. Each point represents a distinct manufacturable stacking sequence satisfying symmetry and balance constraints.

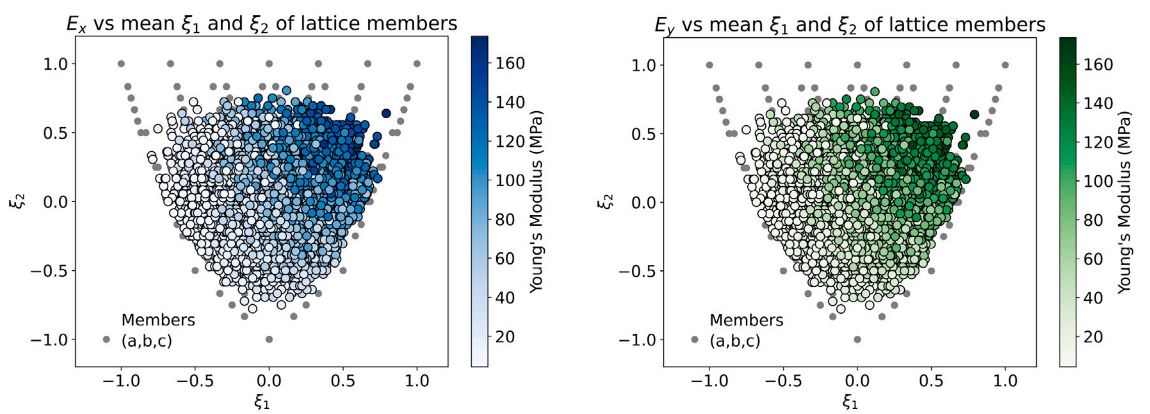

(a) Variation of Elastic modulus E_x (MPa) of the composite lattice as a function of lamination parameters. (b) Variation of Elastic modulus E_y (MPa) of the composite lattice as a function of lamination parameters.

Fig. 6. Elastic modulus distribution in lamination parameter space for 12-ply XN80-epoxy lattices: (a) E_x and (b) E_y. Grey markers show individual member parameters (ξ_1^m, ξ_2^m); coloured markers show lattice-averaged parameters with colour intensity indicating modulus magnitude (20–160 MPa).

where ξ_i^{pred} denotes the predicted lamination parameter vector for member i, and ξ_i^{db} corresponds to the nearest available vector in the database.

The lamination parameter yielding the minimum cumulative distance is selected, and the layup configuration is reconstructed by retrieving the closest layup for each member within the selected tree. In this manner, a set of physically realisable stacking sequences is obtained that most closely approximates the inverse model predictions in lamination parameter space. Since this inverse prediction is performed member-wise, the proposed encoder–decoder can be applied to a wide range of lattices where the members satisfy the composite laminate theory assumptions.

5. Results

5.1. Verification

To verify the equations developed using lamination parameters, a composite lattice structure comprising five plies is considered. The constituent ply properties are based on a unidirectional Glass/Epoxy composite with the following orthotropic parameters: longitudinal modulus $E_{11} = 38\,600$ MPa, transverse modulus $E_{22} = 8270$ MPa, major Poisson's ratio $\nu_{12} = 0.26$ and in-plane shear modulus $G_{12} = 4140$ MPa. The geometry of the lattice is defined by a unit cell with height $h = 50$ mm, length $L = 50$ mm and an effective core thickness derived to achieve a relative density of $\rho^*/\rho_s = 0.0722$. The equivalent elastic properties of the lattice calculated from the developed work is compared against the strain energy based approach developed by Jasotharan et al. [35] and is shown in Table 1

Table 1
Verification of lamination parameter formulation against reference strain energy method. Extensional stiffness components Q_{11}, Q_{12}, and Q_{66} for three representative 5-ply Glass/Epoxy layups show close agreement with [35], with maximum error below 3%.

Layup	Q_{11} N/mm^2		Q_{12} N/mm^2		Q_{66} N/mm^2	
	Ref [35]	Proposed	Ref [35]	Proposed	Ref [35]	Proposed
45,−45,0,−45,45	324.71	324.92	319.85	319.90	2.43	2.51
0,0,90,0,0	595.17	594.53	584.25	585.35	5.46	4.59
90,0,0,0,90	482.53	484.34	478.29	476.86	2.12	3.74

5.2. Lattices in lamination parameter space

For the results in this section, relative density = 0.0722 is used and the geometry is same as the previous section, however the number of plies and orientations are modified along with the composite material. The design space is restricted to only balanced and symmetric laminates for two reasons, (i) ease of manufacturability and (ii) simultaneous simplification of design space. The composite material system used is that of a high-modulus carbon epoxy system (XN80 + Epoxy) [36]. The properties are mentioned in Table 2.

The lamination parameter space formed by composite lattices made of 4 plies and 12 plies are shown in Fig. 5. It can be observed that the balanced and symmetric laminates occupy the well-known parabolic shape and the design space inside this parabola is not continuous. Therefore, selecting points inside the parabolic design space for manufacturability is not trivial and shows the challenges in inverse design of lattices. It is worth mentioning that larger number of plies through the thickness enables a larger designing space for tailoring.

In Figs. 6(a) and 6(b), the lamination space is plotted. The grey dots indicate the lamination parameters of the individual members of the lattice $(\xi_1^a, \xi_1^b, \xi_1^c), (\xi_2^a, \xi_2^b, \xi_2^c)$. The coloured dots indicate mean lamination parameters of the lattice $\xi_1^m = (\xi_1^a + \xi_1^b + \xi_1^c)/3$, $\xi_2^m = (\xi_2^a + \xi_2^b + \xi_2^c)/3$ and the magnitude of the colour show the value of the elastic modulus achieved, E_x and E_y. In this figure, lattice members contain 12 plies but with varying lamination parameters. Therefore, only the orientations of the plies in the laminate are changed with the thickness being constant. The figure reveals the design space for E_x and E_y and combinations thereof that can be achieved. It can be instantly seen that by just refining the lamination parameters one can achieve elastic modulus ranging from 20 MPa to 160 MPa. Furthermore, Figs. 6(a) and 6(b) characterises how the lattice's effective in-plane moduli depend on the first two lamination parameters, which encode the fibre-orientation content of the underlying members. The feasible (ξ_1, ξ_2) region is bounded (as expected from classical laminate theory constraints), and both E_x and E_y increase as designs migrate towards the upper–right sector of this domain.

Fig. 7 describes the anisotropy observed in composite lattices. Fig. 7(a) illustrates the distribution of lamination parameters (ξ_1, ξ_2) corresponding to the members of composite lattices. Similar to Fig. 6, the lamination parameters of an individual laminate member are shown as grey dots. Lattices are generated from this individual members and the lattice members selected from this pool are highlighted as triangular markers, where markers with identical colours belong to the same lattice. Not all the lattice members generated are shown here for clarity. By looking at an example lattice (marked with connected lines in Fig. 7(a)) it can be inferred that how an individual laminate occupy the feasible lamination parameter space. That is, a subset is systematically grouped to form a lattice structure.

Fig. 7(b) presents the anisotropy value in terms of the stiffness ratio E_x/E_y of the members shown in Fig. 6. Here, triangular markers again indicate the selected lattice members, but the colouring encodes the degree of anisotropy, with the colour scale ranging from isotropic configurations ($E_x/E_y = 1.0$) to highly anisotropic ones ($E_x/E_y \approx 1.5$).

The lamination parameters connected by the triangle marked in Fig. 7(a) depict a lattice whose anisotropy is found to be the maximum among configuration tested, as it can be seen from Fig. 7(b). It can be observed that the maximum anisotropy is observed in the lattice where the member lamination parameters are significantly different. Therefore, lattices with members near the periphery of the lamination parameter domain tend to exhibit higher anisotropy. This highlights the extent to which anisotropy varies across the lattice members and makes evident the directional stiffness tailoring achievable through lamination parameter design.

6. Inverse design with lamination-parameter informed encoder–decoder

In this section, the ability of the encoder–decoder to construct lattices based on the input E_x and E_y is demonstrated. Alternatively, one can use E_x and the range of anisotropy required. When a target pair of macroscopic elastic moduli (E_x, E_y), is specified as input, the neural network encoder maps these values onto a set of six latent variables,

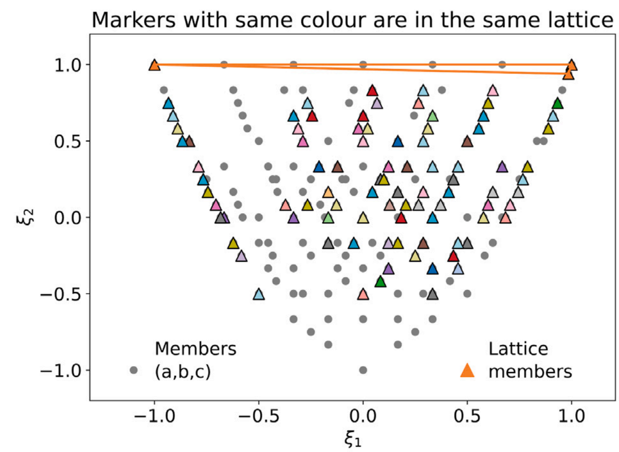

(a) Distribution of lamination parameters of lattice members. An example lattice is marked by a triangle.

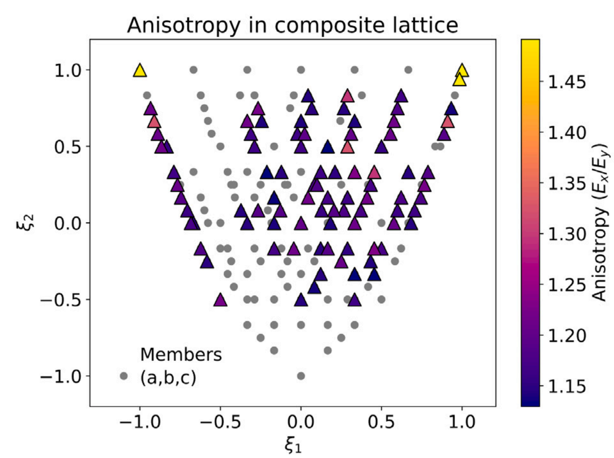

(b) Anisotropy plot of the lattice members

Fig. 7. Anisotropy distribution in composite lattices (a) Grey markers show ξ_i of individual member; Triangular markers indicate members belonging to the same lattice configuration. Connected triangle is a lattice exhibiting maximum anisotropy. (b) Colour intensity represents anisotropy ratio E_x/E_y.

interpreted as the lamination parameters (ξ_{1i}, ξ_{2i}) corresponding to the three lattice members. Each parameter pair is subsequently transformed into a member-level modulus (E_a, E_b, E_c) via closed-form expressions derived from laminate invariants $(U_1, U_2, U_3, U_4, U_5)$. These member moduli are then used to reconstruct the homogenised lattice properties $(\hat{E}_x, \hat{E}_y)$. The training loss enforces agreement between $(\hat{E}_x, \hat{E}_y)$ and the prescribed input values (E_x, E_y) (see Eq. (39)). This ensures that the inferred lamination parameters yield physically consistent stiffness states that reproduce the target anisotropy. This is schematically shown in Eq. (40)

$$(E_x, E_y) \xrightarrow{\text{Encoder}} \{\xi_{1i}, \xi_{2i}\} \xrightarrow{\text{laminate}} \{E_a, E_b, E_c\} \xrightarrow{\text{homogenisation}} (\hat{E}_x, \hat{E}_y). \tag{40}$$

Fig. 8(a) compares the design input E_x with corresponding reconstructed modulus $\hat{E}_x$, while Fig. 8(b) reports the equivalent comparison for E_y, for a selected number of inputs. In both cases, the encoder–

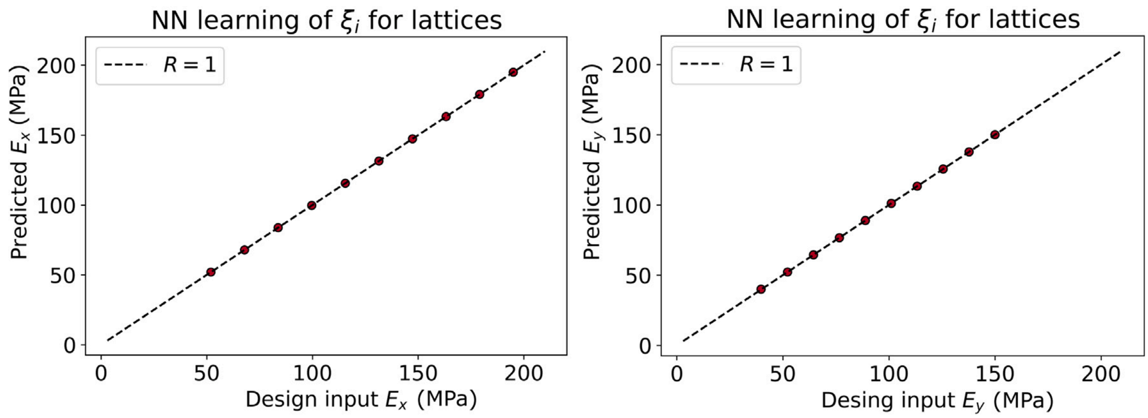

(a) Prediction of E_x (b) Prediction of E_y

Fig. 8. Encoder–decoder prediction accuracy for target elastic moduli: (a) longitudinal modulus E_x and (b) transverse modulus E_y. Red markers show predicted values against design input targets, (dashed line shows $R = 1$).

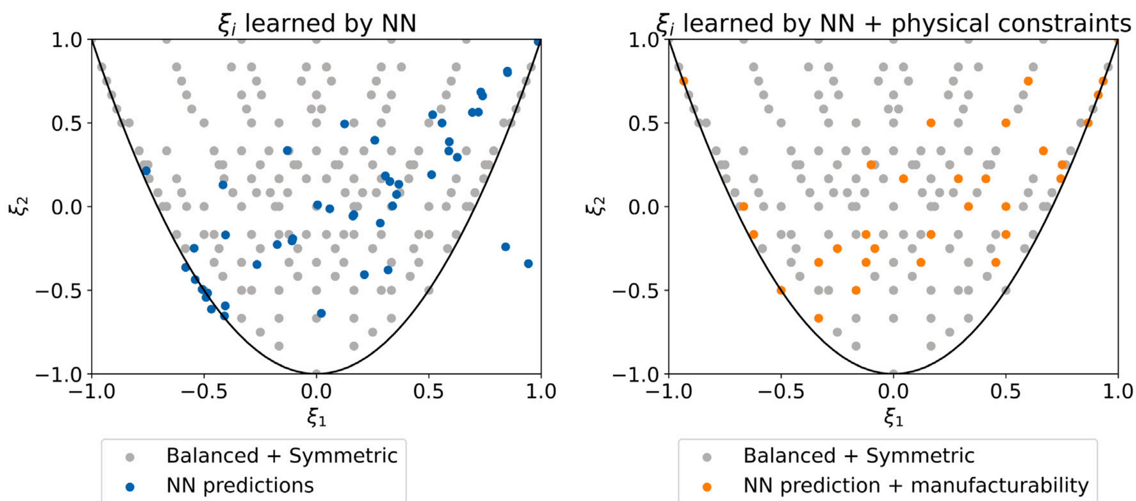

(a) Lamination parameters predicted by the neural network (b) Lamination parameters predicted by neural network and adjusted for manufacturability

Fig. 9. Enforcement of manufacturability constraints in inverse design. (a) Lamination parameters predicted directly by the neural network (blue markers) relative to the admissible design space for balanced and symmetric laminates (grey markers). (b) Adjusted lamination parameters after kd-tree retrieval of nearest manufacturable layups (orange markers).

decoder network is capable of accurately inferring lamination parameters that recover the prescribed stiffness states. It is noted that manufacturability constraints are deliberately excluded during the encoder–decoder training to avoid over-constraining the learning process; instead, these constraints are applied subsequently, once the lamination parameters have been identified.

Fig. 8 compares the lamination parameters predicted by the neural network before and after the imposition of manufacturability constraints. In Fig. 9a, the predicted lamination parameters (blue markers) are shown relative to the admissible design space for balanced and symmetric laminates (grey markers).

To enforce manufacturability, the encoder–decoder predictions, expressed in terms of lamination parameters, are subsequently converted into the corresponding member-level moduli $((E_a, E_b, E_c))$. This is because operating in modulus space reduces the problem of predicting layups to a one-dimensional search for each member modulus, which can be efficiently handled using the KDTree structure.

A library, $\text{Layup}^{\text{lib}}$, containing an exhaustive database of balanced and symmetric layups for a given ply count and the corresponding elastic modulus is generated and stored prior to the inverse design. The mapping from predicted member modulus E_α to a manufacturable layup L_α is achieved via a nearest-neighbour search from this precomputed library:

$$L_\alpha = \text{Layup}^{\text{lib}}_{\underset{j}{\operatorname{argmin}}|E_\alpha - E_j^{\text{lib}}|}, \quad \alpha \in \{a, b, c\}. \tag{41}$$

The retrieved layup L_α contains the orientation of individual plies and since the search is performed over admissible layups, manufacturability is directly enforced. The lamination parameters of the retrieved layup are plotted in Fig. 9(b) and shows that the NN predictions are projected onto discrete admissible points in the lamination parameter space.

Fig. 10 illustrates the neural network predictions of the homogenised lattice properties in comparison with the physically admissible anisotropy bounds. The blue shaded region represents the set of admissible stiffness pairs obtained from enumerated balanced and symmetric laminates, which defines the theoretical design envelope. The red markers correspond to the neural network predictions for selected input cases (from Fig. 8). It is evident that all predictions fall strictly within the admissible region, confirming that the encoder–decoder framework not only reconstructs the target moduli but also respects the anisotropy constraints imposed by laminate theory.

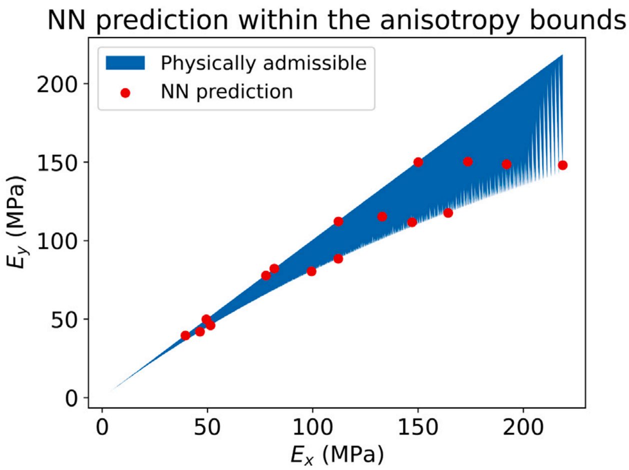

Fig. 10. Neural network predictions within physically admissible anisotropy bounds. The blue shaded region represents all feasible stiffness pairs (E_x, E_y). Red markers show predictions against design targets.

7. Tailoring based on the anisotropy ratio

7.1. Definition and analytical expressions

The anisotropy ratio is defined as the ratio of the equivalent Young's modulus in the longitudinal direction to that in the transverse direction, denoted by E_x/E_y. To obtain this, we begin with the expressions for E_x and E_y, given in Eqs. (9) and (10). The ratio, denoted by m can be expressed as

$$m = \frac{E_x}{E_y} = \frac{\cos^2\theta\left(\alpha^2\left(\sin^2\theta\right)+\cos^2\theta\right)+4\alpha^2\beta\cos^2\theta\frac{\eta_1}{\eta_2(1+\eta_1)}}{(\beta+\sin\theta)^2\left(\alpha^2\cos^2\theta+\sin^2\theta\right)} \tag{42}$$

This form offers a clearer interpretation of the directional stiffness contrast in terms of geometry (α, β, θ) and material disparity ratios (η_1, η_2). The expression highlights how tuning these parameters controls the degree of anisotropy in the architected lattice.

Different values of the anisotropy ratio $m = \frac{E_x}{E_y}$ have clear and compelling physical implications. A value of $m = 1$ corresponds to an elastically isotropic lattice, where stiffness is equal in both principal directions. Values of $m > 1$ indicate increasing longitudinal stiffness relative to transverse stiffness, suitable for applications requiring directional load carrying, such as spars or stiffened skins. Conversely, $m < 1$, down to $m \approx 1/10$, indicates high transverse compliance with respect to axial rigidity—a feature desirable in deployable structures, adaptive morphing skins, and anisotropic damping layers. The ability to analytically target and achieve extreme values of m as low as 0.1 or as high as 10 represents a transformative leap over conventional lattice design strategies. Fig. 11 shows the variation of the anisotropy ratio E_x/E_y as a function of the material disparity ratio η_1 and the cell angle θ for $\alpha = 0.2$, highlighting the combined influence of geometric and material parameters.

Fig. 11(a), ($\beta = 1, \eta_2 = 1$), shows a near-isotropic baseline. Increasing β to 2.5 in (b) enhances longitudinal stiffness and anisotropy. Reducing η_2 in (c) increases stiffness contrast and anisotropy, while (d), ($\beta = 2.5, \eta_2 = 0.1$), exhibits the strongest directional dependence, highlighting the combined effect of geometric and material contrast.

Traditionally, lattice anisotropy could only be modulated through geometric parameters, namely α (thickness-to-length ratio), β (height-to-length ratio), and θ (inclination angle). This restricted the design flexibility and often imposed conflicting trade-offs between stiffness, strength, and manufacturability. The analytical expression derived above enables designers to directly prescribe a target anisotropy ratio $m = \frac{E_x}{E_y}$ and systematically determine the required material contrast between lattice members. This enables reverse engineering of member-level composite properties to achieve system-level performance.

Table 2
Orthotropic material properties for four fibre-epoxy composite systems. The fibre–matrix modulus ratio E_1/E_2 ranges from 4.66 for E-glass to 49.25 for XN80 carbon.

Material	E_1 GPa	E_2 GPa	G_{12} GPa	ν_{12}	E_1/E_2
M55 + Epoxy	277.36	8.1	3.0	0.31	34.2
XN80 + Epoxy	392.0	7.96	2.95	0.31	49.25
Boron + Epoxy	204.0	18.5	5.6	0.23	11.02
E-glass + epoxy	38.6	8.27	4.14	0.26	4.66

7.2. Material selection for lattice anisotropy

In this section, how material selection influences anisotropy of lattices is discussed. It is noted that only hexagonal lattices with uniform relative density and $\theta = 30°$ are considered. The lattice is geometrically isotropic and therefore anisotropy can be introduced only with different materials and its orientation. Therefore, this serves as a test case to select materials to introduce anisotropy.

The critical property in selecting the material for lattice is the longitudinal and transverse direction (material) modulus contrast. Four different materials are considered in this analysis and they are listed in Table 2. While E-glass+epoxy is a well-known composite material, XN80 is a high modulus carbon fibre capable of introducing large differences in the fibre and matrix properties. Correspondingly, it can be read from Table 2 that E_1/E_2 is 4.66 times for E-glass+epoxy, it is close 50 for XN80 carbon fibre based composite. This large magnitude of material anisotropy is the key driver to perform stiffness tailoring in lattices since the design space is enhanced with the use of such materials. To understand this, hexagonal lattices with uniform relative density but with different ply orientations and with materials listed in Table 2 are generated.

Approximately 1 million configurations are generated such that each member has 12 plies and the anisotropy observed in these lattices is shown in Fig. 12. It can be readily observed that the composite material with large magnitude of E_1/E_2 results in larger anisotropy E_x/E_y. Thus, highly anisotropic fibres such as XN80 enable the design of lattice architectures with significant directional tailoring, while material systems such as E-glass limit the achievable anisotropy regardless of configuration.

Although Fig. 12 explains the anisotropy that can be achieved with different materials, it does not show the distribution of anisotropy obtained with the material. To understand this, anisotropy is plotted as a function of lattice longitudinal modulus in Fig. 13. Different straight lines corresponding to different values of E_y and constant slope of these lines indicate that E_y is constant in those lines. Furthermore, for a given value of E_x different values of anisotropy are possible in combination with E_y, as it can be observed in Fig. 13. Critically, the largest value of anisotropy is observed in lattices with larger values of E_x. This is because to increase the disparity between the member modulus, some of the members need to have larger magnitude of elastic modulus.

The selection of composite material has profound implications for the inverse design problem established through the lamination parameter framework. Eq. (42) determines the required material disparity ratios η_1 and η_2, which in turn prescribe target elastic moduli E_a, E_b, and E_c for individual members. Achieving these targets through lamination parameter selection is fundamentally conditioned by material choice. A highly anisotropic material provides an expanded design space. The non-uniqueness inherent in Eq. (37) implies that even within a single material system, multiple layup configurations may yield equivalent member stiffness.

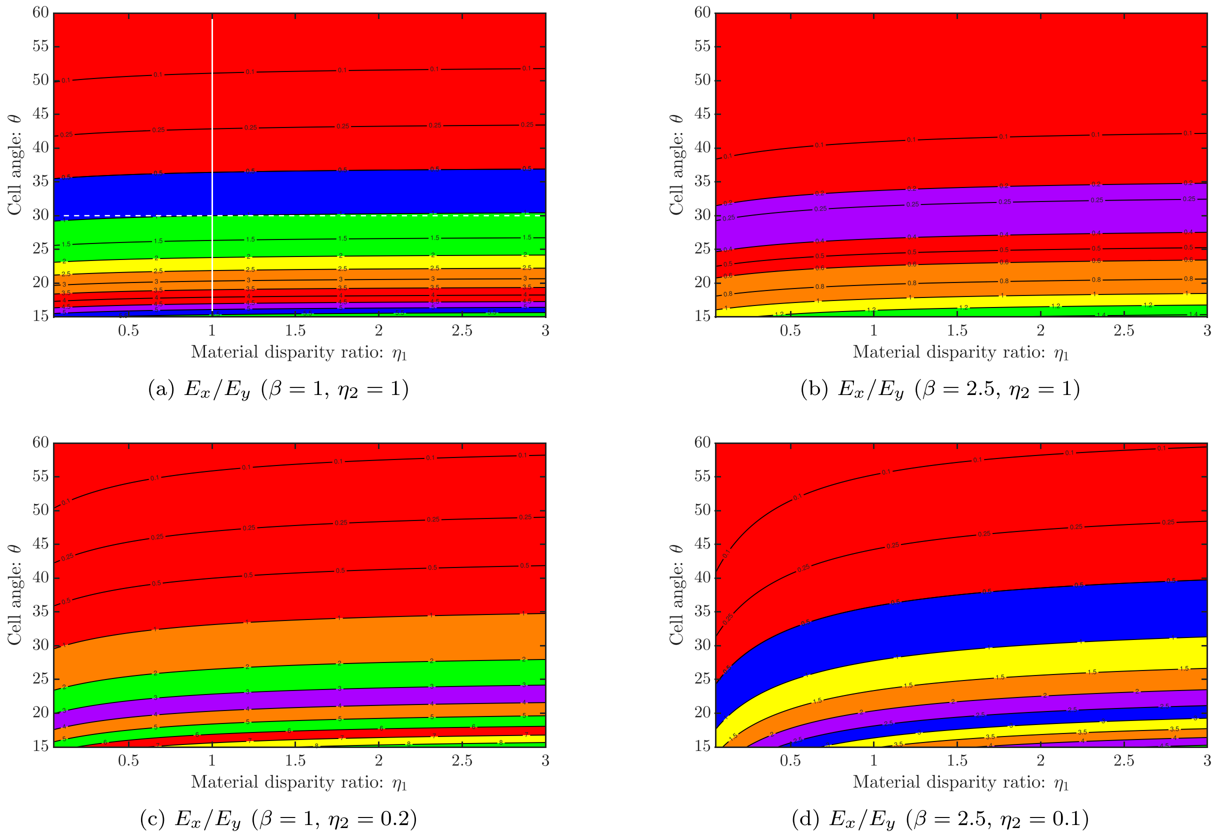

Fig. 11. Contours of anisotropy ratio E_x/E_y plotted as functions of the material disparity ratio (η_1) and the cell angle (θ) for $\alpha = 0.2$ and different values of the height ratio (β) and material disparity ratio η_2. The case corresponding to the classical single-material regular homogeneous lattice ($\beta = \eta_1 = \eta_2 = 1$, $\theta = 30°$) is marked with lines in (a).

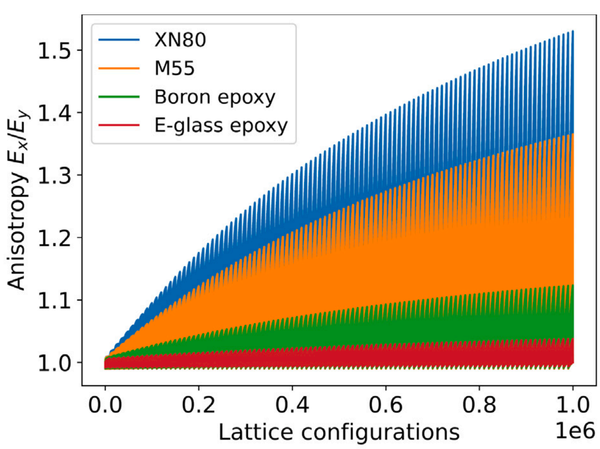

Fig. 12. Influence of material fibre–matrix modulus ratio E_1/E_2 on achievable lattice anisotropy E_x/E_y for hexagonal configurations with uniform relative density and $\theta = 30°$.

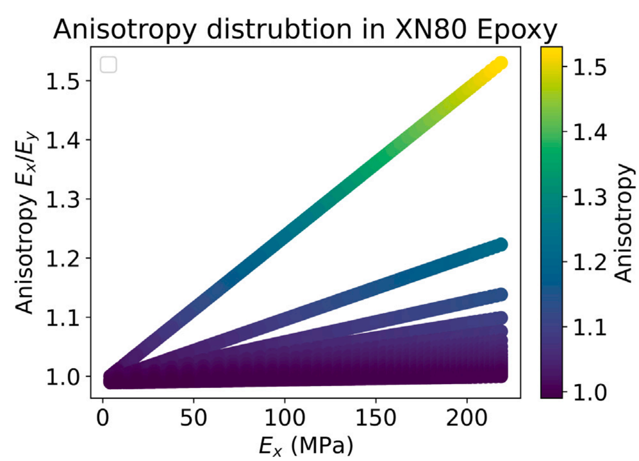

Fig. 13. Relationship between lattice longitudinal modulus E_x and anisotropy ratio E_x/E_y for XN80-epoxy. Each marker is a distinct lattice configuration with colour indicating anisotropy magnitude.

7.3. Variable anisotropy ratio predictions with encoder–decoder

In this section, the ability of encoder-decoder to predict a wide range of anisotropy in hexagonal lattices with XN80 and epoxy material system is described and shown in Table 3. Following the description of the neural network in Section 6, a demonstration resulting in the predictions of layup, starting from the input transverse modulus and the anisotropy range is shown in Table 3. The input transverse modulus is set to $40 \leq E_y \leq 150$ and anisotropy is set as $1.0 \leq E_x/E_y \leq 1.5$. Different lattice configurations are predicted by the NN, among them the key results are listed in Table 3. Following the lamination parameter predictions directly from the NN, layups are calculated from the library E^{lib} using the kD-tree structure. Predictions are performed for lattices with 12 plies as well as 6 plies, showing the versatility of the network. Similar to the observations in Fig. 13, lattices with largest anisotropy is observed when the longitudinal elastic modulus is larger.

The predicted layups shows diverse stacking sequences, ranging from symmetric and balanced configurations (e.g., Design 1a: $[-60, 0, 60, 0, 60, -60, -60, 60, 0, 60, 0, -60]$) to highly polarised orientations

Table 3
Encoder–decoder predictions for variable anisotropy ratios in XN80-epoxy hexagonal lattices. Results demonstrate capability across both 12-ply and 6-ply designs, with predicted anisotropy ranging from near-isotropic (1.10) to highly directional (1.48). Maximum anisotropy configurations occur at higher longitudinal stiffness.

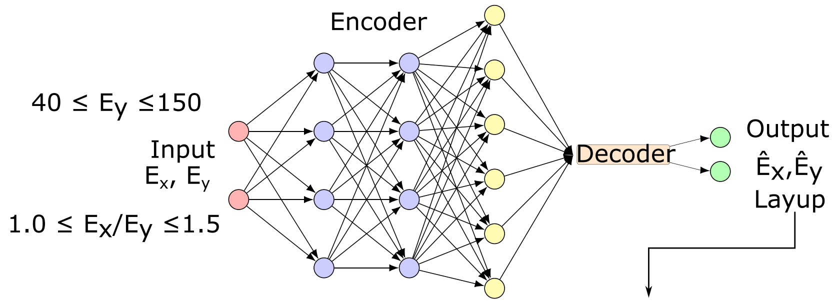

Layup predictions from NN for different anisotropy ratio ($\in$ XN80-Epoxy)

Lattice Output	Member	**Layup predicted by NN and kD-tree**	$\hat{E}_x$	$\hat{E}_y$	**Aniso**
		Design with 12 plies			
	a	[-60, 0, 60, 0, 60, -60, -60, 60, 0, 60, 0, -60]			
1	b	[-30, 30, -75, 15, 75, -15, -15, 75, 15, -75, 30, -30]	56.99	50.41	1.13
	c	[-60, 60, -60, -60, -60, -60, -60, -60, 60, -60]			
	a	[30. 30. 0. 90. -30. 30. 30. -30. 90. 0. 30. 30.]			
2	b	[-45. 15. -15. 45. 0. 90. 90. 0. 45. -15. 15. -45.]	107.68	85.75	1.25
	c	[-60. 60. -60. -60. -60. -60. -60. -60. -60. -60. 60. -60.]			
	a	[-15. 0. 0. 0. 0. 15. 15. 0. 0. 0. 0. -15.]			
3	b	[-15. 0. 0. 0. 0. 15. 15. 0. 0. 0. 0. -15.]	209.9	149.9	1.40
	c	[90. 75. 90. -75. 90. 75. 75. 90. -75. 90. 75. 90.]			
		Design with 6 plies			
	a	[-30. 30. -30. -30. 30. -30.]			
4	b	[90. -15. 15. 15. -15. 90.]	47.40	42.82	1.10
	c	[-60. 60. 60. 60. 60. -60.]			
	a	[30. 0. -30. -30. 0. 30.]			
5	b	[30. 0. -30. -30. 0. 30.]	97.58	79.28	1.23
	c	[-60. 60. 60. 60. 60. -60.]			
	a	[0. 0. 0. 0. 0. 0.]			
6	b	[0. 0. 0. 0. 0. 0.]	218.72	147.6	1.48
	c	[90. -75. 75. 75. -75. 90.]			

dominated by 0° plies (e.g., Design 6a). This distribution illustrates the ability of the framework to explore non-trivial laminate configurations that yield the desired anisotropy targets. Importantly, the use of the encoder–decoder structure enables the mapping of target elastic properties (E_x, E_y) into a feasible laminate design space and retrieve manufacturable stacking sequences through the kD-tree search strategy.

7.4. Fixed anisotropy ratio predictions with encoder–decoder

Similar to Section 7.3, the encoder–decoder predictions for a fixed value of anisotropy and the results are shown in Table 4. The encoder–decoder is provided with the inputs in terms of only E_x and E_y and no prior information. It can be observed that the predictions show that multiple configurations can be obtained for the same value of anisotropy ratio. This is expected since E_x and E_y can be varied and thus a anisotropy ratio can be obtained across different regions (refer Fig. 13). Interestingly, the encoder–decoder predicts this phenomena without any pre-training since physics-based equations are directly embedded in the decoder.

7.5. Upper bound on anisotropy

The maximum value of anisotropy that can be obtained in an isotropic lattice ($\theta = 30°$) is bounded. This can be observed in Fig. 12 where the anisotropy is reaching an asymptote. However, to definitively understand the maximum anisotropy, unidirectional stacking sequences are considered, and this is shown in Table 5. The lattice member are made from either 0° plies or 90° plies. These configurations provide bounds on the stiffness tailoring that can be obtained with a composite material. Table 5 summarises the resulting upper bounds on anisotropy for different fibre–epoxy material systems. High-modulus carbon systems such as XN80/epoxy exhibit the largest anisotropy, while glass fibre systems show behaviour closer to isotropy. In other words, using Glass + epoxy will provide minimal design space for stiffness tailoring. It can be further ascertained that there exists an upper bound for each composite material system and calculating this upper bound as a prior is necessary to design the scope of stiffness tailoring.

Table 4
Multiple layup solutions achieving fixed anisotropy ratio $E_x/E_y \approx 1.3$ at different stiffness levels for 6-ply XN80-epoxy lattices. The encoder–decoder predicts distinct stacking sequences yielding equivalent anisotropy across a range of absolute moduli, from $(E_x, E_y) = (127.68, 97.83)$ MPa to $(179.78, 140.52)$ MPa. This non-uniqueness demonstrates the framework's ability to explore multiple design solutions satisfying identical anisotropy constraints whilst capable of secondary optimisation.

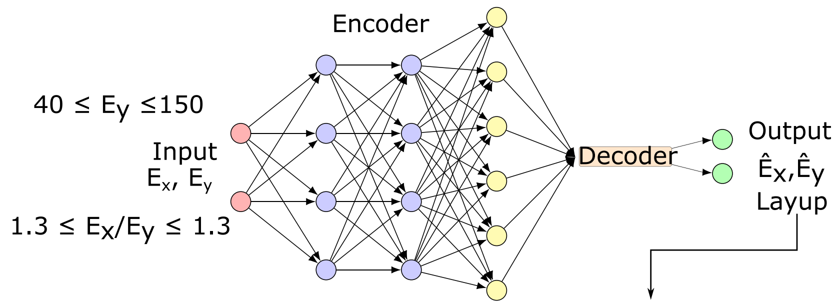

Multiple layups predicted by NN for similar anisotropy ratio
but with different modulus (∈ XN80-Epoxy)

Lattice	Member	**Layup**	E_x	E_y	**Aniso**
Design with 6 plies					
	a	[90. -15. 15. 15. -15. 90.]			
1	b	[90. -15. 15. 15. -15. 90.]	127.68	97.83	1.30
	c	[-60. 60. 60. 60. 60. -60.]			
	a	[15. -15. 15. 15. -15. 15.]			
2	b	[0. 90. 0. 0. 90. 0.]	149.36	112.67	1.32
	c	[90. -75. 75. 75. -75. 90.]			
	a	[-15. 15. 0. 0. 15. -15.]			
2	b	[-15. 15. 0. 0. 15. -15.]	179.78	140.52	1.28
	c	[-45. 45. 45. 45. 45. -45.]			

Table 5
Material-dependent upper bounds on anisotropy for hexagonal lattices ($\theta = 30°$) with extreme unidirectional stacking sequences to establish theoretical maximum directional stiffness contrast achievable through layup design alone.

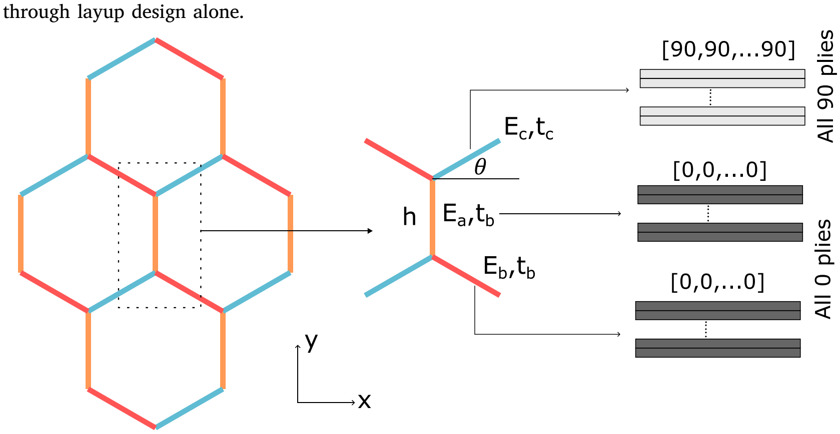

Material System	Maximum anisotropy
XN80 + Epoxy	1.49
M55 + Epoxy	1.34
Boron + Epoxy	1.10
E-glass + Epoxy	1.03

8. Conclusion

This work addressed the combinatorial explosion inherent in composite lattice design by developing a lamination parameter-informed encoder–decoder framework that transforms discrete layup optimisation into continuous property space mapping. We derived closed-form analytical expressions linking homogenised lattice elastic properties to member-level lamination parameters through classical laminate theory and homogenisation mechanics, eliminating the need for iterative finite element analysis. The encoder, implemented as a feed-forward neural network, learns to map target effective moduli (E_x, E_y) to physically admissible lamination parameters, while the decoder enforces mechanical consistency through embedded analytical relations rather than data-driven approximation. This architecture successfully performs inverse design, predicting manufacturable stacking sequences for prescribed stiffness and anisotropy targets through efficient kd-tree retrieval, and was validated across hexagonal lattice configurations spanning 4 to 12 plies with multiple composite material systems. The principal novel contributions include:

1. Analytical homogenisation of composite lattices expressed entirely through lamination parameters, providing the first continuous design space representation for multi-member periodic architectures.
2. Physics-informed decoder architecture embedding closed-form mechanics equations that guarantee physical admissibility without requiring extensive training datasets.
3. Unified inverse design framework integrating neural network prediction with manufacturing constraint enforcement through post-processing projection and discrete layup retrieval.
4. Analytical derivation of anisotropy ratio as an explicit function of material disparity ratios and geometric parameters, enabling direct prescription of directional stiffness targets.
5. Establishment of material-dependent upper bounds on achievable anisotropy, demonstrating that maximum directional tailoring scales with both fibre-matrix modulus contrast and absolute lattice stiffness.

These results enable aerospace structural designers to rapidly explore composite lattice configurations that were previously inaccessible due to computational cost, directly targeting anisotropic stiffness distributions required for morphing skins, adaptive structures, and multifunctional load-bearing systems. The framework provides a template for integrating domain-specific physics with machine learning in inverse materials design problems where governing equations are known but solution space is intractable. Future work will focus on experimental validation to manufacture representative lattice specimens and conduct mechanical tests to further validate the predictive abilities of the framework, similar to the works in the literature [28]. Future extensions will address three-dimensional lattice topologies beyond planar hexagonal arrays, incorporate failure criteria and strength constraints alongside stiffness targets, integrate buckling resistance as a design objective, and validate predictions through additive manufacturing and mechanical testing of physical specimens across the predicted design envelope.

CRediT authorship contribution statement

Jagan Selvaraj: Writing – original draft, Software, Methodology, Investigation, Formal analysis, Conceptualization. **Sondipon Adhikari:** Writing – review & editing, Writing – original draft, Software, Resources, Methodology, Investigation, Conceptualization.

Declaration of competing interest

The authors declare that they have no known competing financial interests or personal relationships that could have appeared to influence the work reported in this paper.

Acknowledgement

The authors would like to acknowledge the financial support provided by the Univeristy of Glasgow's James Watt School of Engineering.

Data availability

The data used in this research is included within the article.

References

[1] Wang Y, Thorn TD, Liu Y, Advani SG, Papageorgiou DG, Bilotti E, Zhang H. A review on energy-efficient manufacturing for high-performance fibre-reinforced composites. Composites A 2025;192:108779. http://dx.doi.org/10.1016/j.compositesa.2025.108779.

[2] Hsissou R, Seghiri R, Benzekri Z, Hilali M, Rafik M, Elharfi A. Polymer composite materials: A comprehensive review. Compos Struct 2021;262:113640. http://dx.doi.org/10.1016/j.compstruct.2021.113640.

[3] Davis SJ, et al. Net-zero emissions energy systems. Science 2018;360(6396):eaas9793.

[4] Gibson LJ, Ashby MF. Cellular solids: Structure and properties. 2nd ed. Cambridge University Press; 1997.

[5] Hunt CJ, Morabito F, Grace C, Zhao Y, Woods BK. A review of composite lattice structures. Compos Struct 2022;284:115120. http://dx.doi.org/10.1016/j.compstruct.2021.115120.

[6] Wickramasinghe JK, Cooper JE, Patel MH. Review of morphing skin technologies for aircraft structures. Proc Inst Mech Eng G 2012;226(4):554–67.

[7] Carey S, McHale C, Weaver PM. A variable-topology morphing composite cylindrical lattice. Compos Struct 2021;276:114542. http://dx.doi.org/10.1016/j.compstruct.2021.114542.

[8] Gong C, Ritchie RO, Wei X, Liu Q, Xiong J. Mechanical properties of modular assembled composite lattice architecture. J Mech Phys Solids 2025;195:105967. http://dx.doi.org/10.1016/j.jmps.2024.105967.

[9] Chen Y, Ye L, Dong H. Lightweight 3D carbon fibre reinforced composite lattice structures of high thermal-dimensional stability. Compos Struct 2023;304:116471. http://dx.doi.org/10.1016/j.compstruct.2022.116471.

[10] Bekas D, Hou Y, Liu Y, Panesar A. 3D printing to enable multifunctionality in polymer-based composites: A review. Composites B 2019;179:107540. http://dx.doi.org/10.1016/j.compositesb.2019.107540.

[11] Fan H-T, Wang H, Chen X-H. An optimization method for composite structures with ply-drops. Compos Struct 2016;136:650–61. http://dx.doi.org/10.1016/j.compstruct.2015.11.003.

[12] Selvaraj J, El Said B. Multiscale modelling of strongly heterogeneous materials using geometry informed clustering. Int J Solids Struct 2023;280:112369. http://dx.doi.org/10.1016/j.ijsolstr.2023.112369.

[13] Mercier S, Molinari A. Homogenization of elastic–viscoplastic heterogeneous materials: Self-consistent and Mori-Tanaka schemes. Int J Plast 2009;25(6):1024–48. http://dx.doi.org/10.1016/j.ijplas.2008.08.006.

[14] Balasubramani N, Zhang B, Chowdhury N, Mukkavilli A, Suter M, Pearce G. Micro-mechanical analysis on random RVE size and shape in multiscale finite element modelling of unidirectional FRP composites. Compos Struct 2022;282:115081. http://dx.doi.org/10.1016/j.compstruct.2021.115081.

[15] Daghia F, Lagache A, Di Gennaro L. Validation of a new viscoelastic model for unidirectional polymer matrix composites by analytical and numerical homogenisation. Eur J Mech A Solids 2023;100:104975. http://dx.doi.org/10.1016/j.euromechsol.2023.104975.

[16] Catalanotti G. On the generation of RVE-based models of composites reinforced with long fibres or spherical particles. Compos Struct 2016;138:84–95. http://dx.doi.org/10.1016/j.compstruct.2015.11.039.

[17] Albazzan MA, Harik R, Tatting BF, Gürdal Z. Efficient design optimization of nonconventional laminated composites using lamination parameters: A state of the art. Compos Struct 2019;209:362–74. http://dx.doi.org/10.1016/j.compstruct.2018.10.095.

[18] Setoodeh S, Abdalla MM, Gürdal Z. Design of variable–stiffness laminates using lamination parameters. Composites B 2006;37(4):301–9. http://dx.doi.org/10.1016/j.compositesb.2005.12.001.

[19] Demir E, Yousefi-Louyeh P, Yildiz M. Design of variable stiffness composite structures using lamination parameters with fiber steering constraint. Composites B 2019;165:733–46. http://dx.doi.org/10.1016/j.compositesb.2019.02.004.

[20] Wu Z, Raju G, Weaver PM. Optimization of postbuckling behaviour of variable thickness composite panels with variable angle tows: Towards "Buckle-Free" design concept. Int J Solids Struct 2018;132–133:66–79. http://dx.doi.org/10.1016/j.ijsolstr.2017.08.037.

[21] Thomas MA, Hallett SR, Weaver PM. Design considerations for variable stiffness, doubly curved composite plates. Compos Struct 2020;244:112170. http://dx.doi.org/10.1016/j.compstruct.2020.112170.

[22] Ntourmas G, Glock F, Daoud F, Schuhmacher G, Chronopoulos D, Özcan E. Mixed Integer Linear Programming formulations of the stacking sequence and blending optimisation of composite structures. Compos Struct 2021;264:113660. http://dx.doi.org/10.1016/j.compstruct.2021.113660.

[23] Sprengholz M, Traub H, Sinapius M, Dähne S, Hühne C. Rapid transformation of lamination parameters into stacking sequences. Compos Struct 2021;276:114514. http://dx.doi.org/10.1016/j.compstruct.2021.114514.

[24] Riley K, Jhon M, Ferrand HL, Wang D, Arrieta A. Inverse design of bistable composite laminates with switching tunneling method for global optimization. Commun Eng 2024;3:115. http://dx.doi.org/10.1038/s44172-024-00260-x.

[25] Raissi M, Perdikaris P, Karniadakis G. Physics-informed neural networks: A deep learning framework for solving forward and inverse problems involving nonlinear partial differential equations. J Comput Phys 2019;378:686–707. http://dx.doi.org/10.1016/j.jcp.2018.10.045.

[26] Wang Y, Soutis C, Ando D, Sutou Y, Narita F. Application of deep neural network learning in composites design. Eur J Mater 2022;2(1):117–70. http://dx.doi.org/10.1080/26889277.2022.2053302.

[27] Li Y, Wan D, Wang Z, Hu D. Physics-constrained deep learning approach for solving inverse problems in composite laminated plates. Compos Struct 2024;348:118514. http://dx.doi.org/10.1016/j.compstruct.2024.118514.

[28] Wang X, Zeng Y, Wang H, Cai Y, Li E, Li G. Data-driven inverse method with uncertainties for path parameters of variable stiffness composite laminates. Struct Multidiscip Optim 2022;65(3):91. http://dx.doi.org/10.1007/s00158-022-03185-1.

[29] Sun H, Wang X, Li J, Li Z, Guan Z. Efficient property-oriented design of composite layups via controllable latent features using generative VAE. Compos Sci Technol 2025;259:110936. http://dx.doi.org/10.1016/j.compscitech.2024.110936, URL https://www.sciencedirect.com/science/article/pii/S0266353824005062.

[30] Zhou H, Zhang DZ, He N, Zhao M. Topology optimization of multi-morphology composite lattice structure with anisotropy properties. Compos Struct 2023;321:117294. http://dx.doi.org/10.1016/j.compstruct.2023.117294.

[31] Peng X-L, Xu B-X. Data-driven inverse design of composite triangular lattice structures. Int J Mech Sci 2024;265:108900. http://dx.doi.org/10.1016/j.ijmecsci.2023.108900, URL https://www.sciencedirect.com/science/article/pii/S0020740323008020.

[32] Mukherjee S, Adhikari S. The mechanics and optimal design of micro-architectured stepped hexagonal lattices. Compos Struct 2023;313:116900.

[33] Adhikari S. The in-plane mechanical properties of highly compressible and stretchable 2D lattices. Compos Struct 2021;272:114167. http://dx.doi.org/10.1016/j.compstruct.2021.114167, URL https://www.sciencedirect.com/science/article/pii/S0263822321006292.

[34] Bloomfield M, Diaconu C, Weaver P. On feasible regions of lamination parameters for lay-up optimization of laminated composites. Proc R Soc A: Math Phys Eng Sci 2008;465(2104):1123–43. http://dx.doi.org/10.1098/rspa.2008.0380.

[35] Sriharan J, Dias M, Fernando D, Adhikari S. A unified approach for the prediction of the effective properties of laminated composite cellular core. Eng Struct 2024;299:117106. http://dx.doi.org/10.1016/j.engstruct.2023.117106.

[36] Design and characterisation of advanced pseudo-ductile unidirectional thin-ply carbon/epoxy–glass/epoxy hybrid composites. Compos Struct 2016;143:362–70. http://dx.doi.org/10.1016/j.compstruct.2016.02.010.